A DC–DC Multiport-Converter-Based Solid-State Transformer Integrating Distributed Generation and Storage

Sixifo Falcones, *Member, IEEE*, Rajapandian Ayyanar, *Senior Member, IEEE*, and Xiaolin Mao, *Member, IEEE*

Abstract—The Solid-state transformer (SST) has been proposed by researchers to replace the regular distribution transformer in the future smart grid. The SST provides ports for the integration of storage and distributed generation (DG), e.g., photovoltaic (PV), and enables the implementation of power quality features. This paper proposes a SST topology based on a quad-active-bridge (QAB) converter which not only provides isolation for the load, but also for DG and storage. A gyrator-based average model is developed for a general multiactive-bridge (MAB) converter, and expressions to determine the power rating of the MAB ports are derived. These results are then applied to analyze the QAB converter. For the control of the dc–dc stage of the proposed QAB-based SST integrating PV and battery, a technique that accounts for the cross-coupling characteristics of the QAB converter in order to improve the regulation of the high-voltage-dc link is introduced. This is done by transferring the disturbances onto the battery. The control loops are designed using single-input single-output techniques with different bandwidths. The dynamic performance of the control strategy is verified through extensive simulation and experimental results.

Index Terms—DC–DC converter, distributed generation, multiport converter, smart grid, solid-state transformer.

I. INTRODUCTION

IN THE LAST decade, the smart grid concept has drawn the attention of researchers and the industry as a feasible solution to the challenges that the electrical system is facing due to the growth in load, the increasing penetration of renewables, and the deployment of the distributed generation at the consumer end [1]. The power-electronics-based transformer, or so-called solid-state transformer (SST), is one of the key components of the distribution system proposed by Future Renewable Electric Energy Delivery and Management Systems Center [2].

Besides serving as a regular distribution transformer, the SST provides ports for the proper integration of distributed generation (DG) and energy storage, thus enhancing the reliability
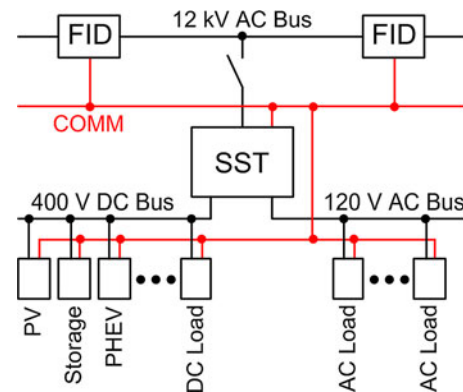
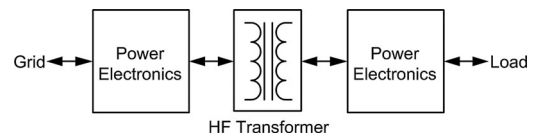Fig. 1. SST with integration of DG, storage, and intelligent loads.

Fig. 2. Basic SST structure.

of the distribution system [3]. Additionally, the SST enables the implementation of distributed intelligence through a secure communication network (COMM) to ensure the stability and optimal operation of the distribution system. Fig. 1 shows the SST interfacing photovoltaic (PV) generation, storage, dc and ac loads, as well as plug-in hybrid electric vehicles (PHEV). The fault identification device (FID) is used for protecting the SST [4]. The basic structure of an SST is shown in Fig. 2.

Besides the advantage of having reduced size and weight due to the use of a high-frequency (HF) transformer [5], the SST makes use of state-of-the-art control techniques that allows it to provide additional functionalities such as on-demand reactive power support to grid, current limiting, and storage management. Harmonics and poor power factor at the load side are isolated from the grid side, thus the overall losses in the distribution system may be reduced.

The selection of the appropriate topology for the SST implementation is a key aspect. In [6], the issue is addressed by comparing six SST topologies based on switch count, losses, and functional capabilities. The three-stage configuration based on a dual-active-bridge (DAB) converter has been identified as a potential candidate for the SST implementation. This topology relies on a low-voltage-dc (LVDC) link for PV and storage integration [7], [8]. This is achieved through separate
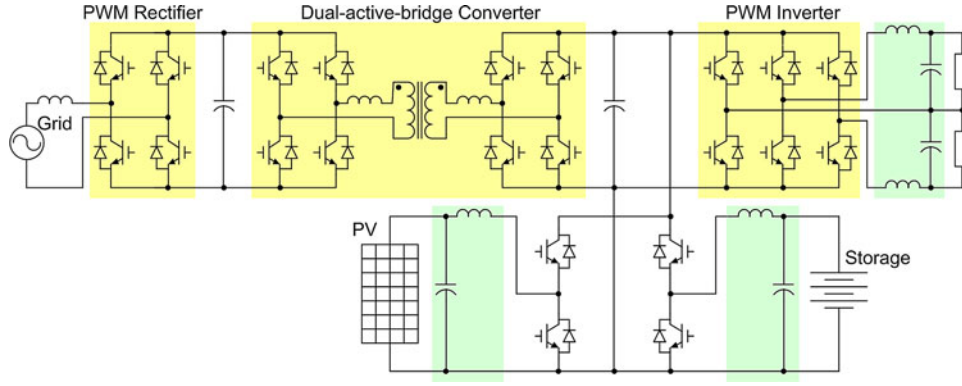
Fig. 3. DAB-based SST with PV and storage integrated through separate converters.
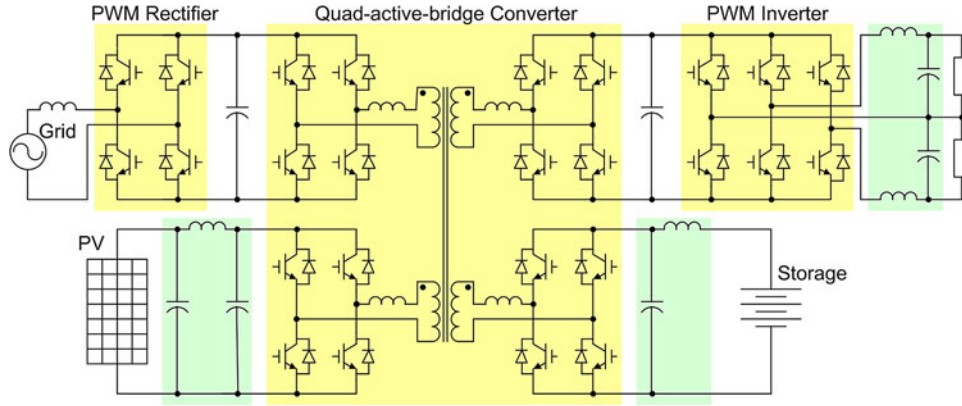

Fig. 4. QAB-based SST with PV and storage integrated through HF transformer.

nonisolated dc–dc converters as seen in Fig. 3. The voltage rating of these converters must be selected mainly based on the LVDC voltage. If their voltage ratings are significantly different from the LVDC voltage and/or isolation is required for grounding, then additional HF transformers may be needed, thus increasing the size of the system. Furthermore, separate controllers for each dc–dc converter are to be designed. To ensure the stability of the controllers, their interaction may need to be examined.

The need of technology for integrating DG and storage into the distribution system has motivated the development of a new generation of power converters. A family of multiport dc–dc converters, which includes the multiactive-bridge (MAB) converters, has been proposed by researchers [9]. Their advantage lies in the integration of several sources with minimum dc–dc conversion stages, which yields a higher power density. Since the SST considered herein includes the grid, the load, the PV system, and the storage, a four-port dc–dc converter as the quad-active-bridge (QAB) converter is required.

This paper proposes the development of a SST based on a QAB converter, to integrate DG and storage. The QAB converter, used in the implementation of the SST dc–dc stage, provides isolation for DG and storage through a single four-winding HF transformer as seen in Fig. 4 and the control design involves the analysis of only a single converter.

II. MAB CONVERTERS

The MAB converters have recently gained the attention of researchers as potential solutions for the integration of renewables with isolation [9]–[14]. The advantages of this type of converters are: interconnection of sources with different voltage ratings by adjusting the HF transformer turn ratios, integrated controller design, zero-voltage switching (ZVS) capability, and high-power density. On the other side, the complexity of the HF transformer and the controller design considerably increases with the number of ports. An n-port MAB converter is comprised of n full-bridge modules magnetically coupled through an n-winding HF transformer as illustrated in Fig. 5. The power that flows between any two ports is mainly controlled through phase-shift-modulation of the square-wave voltages generated by their corresponding full-bridge modules.

The DAB converter introduced in [10] and shown in Fig. 3 can be considered the simplest MAB converter. The equation derived therein for the DAB cycle-by-cycle average (CCA) power can be extended to any MAB converter. Thus, the CCA power transferred from port j into port k of an MAB converter is given by

$$P_{jk} = \frac{V_j' V_k'}{2\pi f_s L_{jk}} \phi_{jk} \left(1 - \frac{|\phi_{jk}|}{\pi} \right), \quad \phi_{jk} = \phi_j - \phi_k \quad (1)$$

where ϕ_j and ϕ_k are the corresponding phase-shift angles, respectively; V_j' and V_k' are the corresponding dc voltages referred
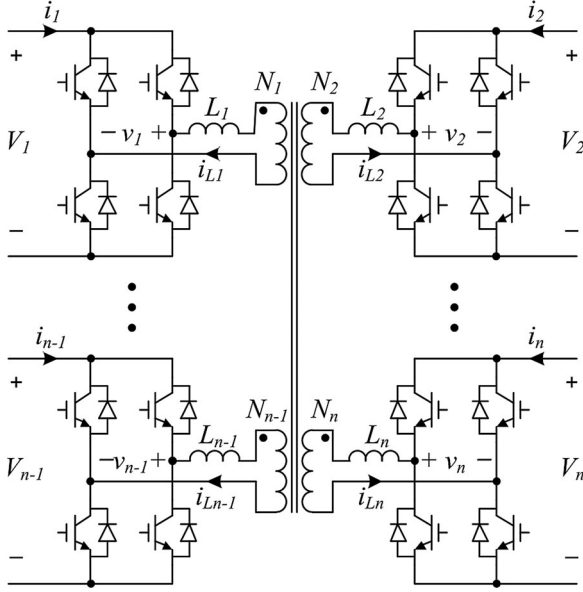
Fig. 5.   Generalized MAB switching model.
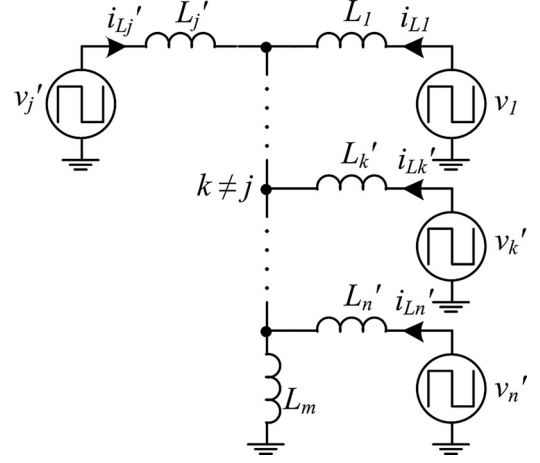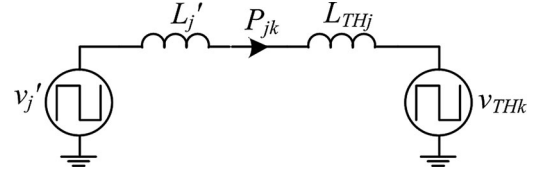

Fig. 6.   MAB "Y" equivalent ac circuit referred to port 1.

Fig. 7.   Thevenin-equivalent AC circuit between MAB ports j and k referred to port 1.

to port 1, respectively; f_s is the switching frequency; and L_{jk} is the equivalent inductance between ports j and k and it is required in order to make use of the equation for the DAB CCA power. L_{jk} also referred to as the link inductance herein, is visualized through a "Δ" equivalent circuit and its calculation is derived in the next section.

A. MAB Link Inductances

The inductor L_j placed on the ac side of port j, i.e., where the high-frequency square-wave voltage v_j is generated, represents the effect of the corresponding winding self-leakage inductance combined with an external inductor. For simplicity, the effects of the mutual-leakage inductances within the HF transformer are not considered herein. A more detailed model for the HF transformer, as in [15], would be worth considering in a future work. For convenience, the magnetizing inductance L_m and the link inductances L_{jk} are defined at port 1. The ac side of the MAB converter in Fig. 5 can be represented by the "Y" equivalent circuit in Fig. 6, where the generated ac voltages and ac currents, and the inductances have been reflected to port 1 according to

$$v'_j = \frac{N_1}{N_j}v_j, \quad i'_j = \frac{N_j}{N_1}i_j, \quad L'_j = \left(\frac{N_1}{N_j}\right)^2 L_j \quad (2)$$

respectively. If port j is selected as the sending port, and port k is selected as the receiving port, where $k = j$, then a Thevenin-equivalent ac circuit can be obtained between these two ports as seen in Fig. 7.

The Thevenin-equivalent inductance $L_{\mathrm{TH}j}$, defined at port 1, is associated with port j since it remains the same for any port k selected as the receiving port. $L_{\mathrm{TH}j}$ is calculated to be

$$L_{\mathrm{TH}j} = \left(\frac{1}{L_m} + \sum_{k \neq j}^{n} \frac{1}{L'_k}\right)^{-1}. \quad (3)$$

Likewise, the Thevenin-equivalent ac voltage $v_{\mathrm{TH}k}$, defined at port 1 and associated with port k, is given by

$$v_{\mathrm{TH}k} = \frac{\left(\frac{1}{L_m} + \sum_{l \neq j, k}^{n} \frac{1}{L'_l}\right)^{-1}}{L'_k + \left(\frac{1}{L_m} + \sum_{l \neq j, k}^{n} \frac{1}{L'_l}\right)^{-1}} v'_k. \quad (4)$$

The CCA power P_{jk} transferred from port j into port k can be expressed as

$$P_{jk} = \frac{V'_j V_{\mathrm{TH}k}}{2\pi f_s \left(L'_j + L_{\mathrm{TH}j}\right)} \phi_{jk}\left(1 - \frac{|\phi_{jk}|}{\pi}\right). \quad (5)$$

Alternatively, P_{jk} can also be calculated from (1). Hence, by simple inspection, the link inductance between these two ports is found to be

$$L_{jk} = \left(L'_j + L_{\mathrm{TH}j}\right)\left[L'_k\left(\frac{1}{L_m} + \sum_{l \neq j, k}^{n} \frac{1}{L'_l}\right) + 1\right]. \quad (6)$$

As a result, the ac side of the MAB converter in Fig. 5 can also be represented by the "Δ" equivalent circuit shown in Fig. 8. This representation resembles an ac transmission system with the link inductors interconnecting the ac voltages. The total number of links within the MAB converter is found to be

$$\#\text{links} = C(n, 2) = \frac{n!}{2!(n-2)!}. \quad (7)$$

This shows that the complexity of the MAB converter dramatically increases with number of ports.
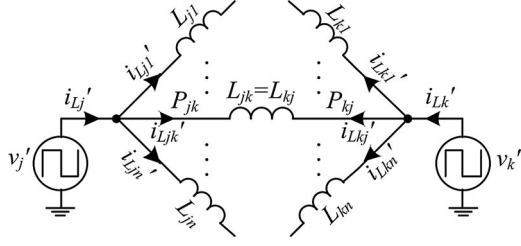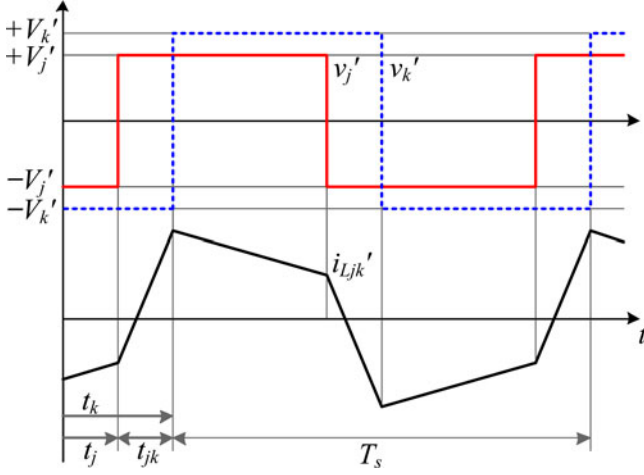
Fig. 8.   MAB "Δ" equivalent AC circuit referred to port 1.

Fig. 9.   Link-inductor ac current between MAB ports j and k referred to port 1.

The ac current i'_{Ljk} through the link inductor L_{jk} flows from port j into port k and its waveform can be generated with the corresponding ac voltages, v'_j and v'_k, as seen in Fig. 9. As a result, by the Superposition principle, the ac current i'_{Lj} through the inductor L'_j is given by

$$i'_{Lj} = \sum_{k \neq j}^{n} i'_{Ljk}. \tag{8}$$

B. Gyrator-Based MAB Average Model

The purpose of this section is to obtain an average model for an MAB converter that characterizes the interaction between its ports as seen from the dc side. In [16], Ehsani *et al.* apply the Gyrator theory to the DAB converter. Therein, the DAB converter is recognized as a natural gyrator converter since the CCA current at the dc side of a port is proportional to the voltage of the dc voltage of the opposite port. The involved proportionality gain is called the gyration gain. The same concept can be extended to the MAB converters. This allows the CCA current at the dc side of any port to be represented as a linear combination of the dc voltages of the remaining ports. For the MAB average model, the CCA value of the pulsating current i_j at the dc side of port j is defined as I_j. The portion of I_j that is generated by port k, defined as I_{jk}, is given by

$$I_{jk} = \frac{P_{jk}}{V_j} = \frac{N_1^2}{N_j N_k} \frac{V_k}{2\pi f_s L_{jk}} \phi_{jk} \left(1 - \frac{|\phi_{jk}|}{\pi}\right). \tag{9}$$
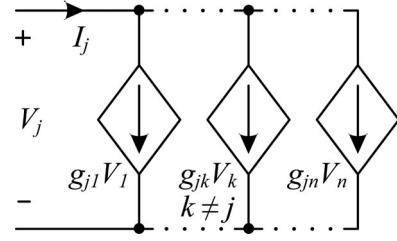
Fig. 10.   Gyrator-based average model for the DC side of MAB port j.

Furthermore, the associated gyration gain is calculated as

$$g_{jk} = \frac{I_{jk}}{V_k} = \frac{N_1^2}{N_j N_k} \frac{1}{2\pi f_s L_{jk}} \phi_{jk} \left(1 - \frac{|\phi_{jk}|}{\pi}\right). \tag{10}$$

Consequently, by the Superposition principle, I_j can be expressed as

$$I_j = \sum_{k \neq j}^{n} I_{jk} = \sum_{k \neq j}^{n} g_{jk} V_k. \tag{11}$$

The resulting gyrator-based average model for the jth port of an MAB converter is illustrated in Fig. 10. This model can be extended to multihalf-bridge converters, as in [17] and [18], after using the appropriate scaling factors for the voltages. From the above equations, it can be observed that $P_{kj} = -P_{jk}$, $L_{kj} = L_{jk}$, and $g_{kj} = -g_{jk}$.

C. MAB Port Power Rating

A power-flow analysis of the MAB converter for each possible operating condition is necessary in order to determine the power rating of its ports. Under a particular power-flow scenario, the MAB converter is assumed to operate at its maximum (max) power when at least one phase-shift angle reaches the allowed magnitude. The power rating of an MAB port is constrained by the scenario that results in the max power flowing into or from it. Therefore, the power rating of the full bridge of an MAB port may depend on the number of sources and loads as well as whether their power flow is restricted to one direction.

If a nonlinearity $\psi(\phi)$ is defined as

$$\psi(\phi) = \phi \left(1 - \frac{|\phi|}{\pi}\right) \tag{12}$$

then, the maximum power that can flow from port j into port k can be expressed as

$$P_{jk\_\max} = \frac{d_j d_k V_1^2}{2\pi f_s L_{jk}} \psi(\phi) \tag{13}$$

where ϕ is a design parameter that represents the allowable magnitude for all MAB phase-shift angles, and $d_j = V'_j/V_1$ and $d_k = V'_k/V_1$ are the dc-conversion ratios of ports j and k, respectively.

When the dc-conversion ratio approximates to one, the DAB converter is shown to achieve ZVS operation of at light loads in [10]. For a wide operating range of a dc conversion ratio, a duty-ratio control technique to ensure ZVS is presented for the triple-active-bridge (TAB) converter and later generalized for
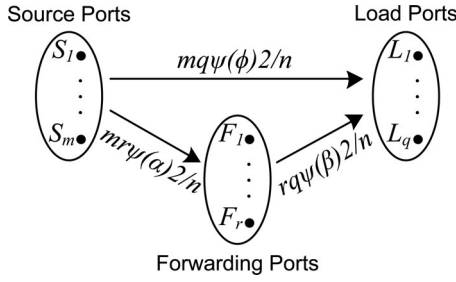
Fig. 11. MAB power flow among source, load, and forwarding ports at max power levels.

any MAB converter in [11]. Another duty-ratio control technique is proposed in [12] in order to minimize the overall TAB converter losses. According to [14], the QAB converter can operate in a DAB mode by disabling two of its ports. In general, an MAB converter can operate in a DAB mode by disabling $n - 2$ ports.

For simplicity, it is assumed herein that

$$d_j = \frac{V_j'}{V_1} = 1, \quad L_j' = L_1 \quad \forall j \in [1, \, n], \; L_m = \infty. \quad (14)$$

By combining (6) and (14), it follows that any MAB link inductance is simplified as

$$L_{jk} = nL_1. \quad (15)$$

Furthermore, by combining (13) and (14), the max power that can flow between any two MAB ports, $P_{\mathrm{MAB\_Link\_max}}$, also referred to as max MAB link power hereinafter, can be simply expressed as

$$P_{\mathrm{MAB\_Link\_max}} = \frac{2}{n} P_{\mathrm{DAB\_max}} \quad (16)$$

where $P_{\mathrm{DAB\_max}}$ is the max power that can flow when the MAB converter operates in a DAB mode. The max MAB link power in per unit is given by

$$P_{\mathrm{MAB\_Link\_max\_pu}} = \frac{P_{\mathrm{MAB\_Link\_max}}}{P_{\mathrm{Base}}} = \frac{2}{n} \psi(\phi)$$

$$P_{\mathrm{Base}} = \frac{V_1^2}{2\pi f_s L_{\mathrm{DAB}}} \quad (17)$$

where $L_{\mathrm{DAB}} = 2L_1$ according to (15).

Intuitively, the maximum power delivered by a source port takes place when the magnitude of the phase-shift angles between it and the load ports reach the allowed value ϕ. Furthermore, a source port can further increase its throughput by redirecting power through passive ports, i.e., those ports with zero-net-power flow, referred to as forwarding ports hereinafter. In general, the power flow for a MAB converter operating with m source ports, q load ports, and r forwarding ports at max power levels is depicted in Fig. 11, where the links represent the total power transferred between two sets of ports, α is the required magnitude for the phase-shift angles between the forwarding ports and the source ports, and β is the required magnitude for the phase-shift angles between the forwarding ports and the load ports.

Under the conditions summarized in Fig. 11, it can be noted that

$$\phi = \alpha + \beta, \quad n = m + q + r. \quad (18)$$

For zero-net-power flow at the forwarding ports, it is found that

$$\beta = \psi^{-1}\left(\frac{m}{q}\psi(\alpha)\right) \quad (19)$$

which can be used in combination with (18) to solve for α and β. For the particular case when $m = q$, then $\beta = \alpha = \phi/2$. The total max MAB power in per unit transferred from the source ports into the load ports is given by

$$P_{\mathrm{MAB\_max\_pu}} = \frac{2m}{n}[q\psi(\phi) + r\psi(\alpha)]$$

$$= \frac{2q}{n}[m\psi(\phi) + r\psi(\beta)]. \quad (20)$$

Consequently, the per-unit max power for each source port is found to be

$$P_{\mathrm{MAB\_S\_max\_pu}} = \frac{2}{n}[q\psi(\phi) + r\psi(\alpha)]. \quad (21)$$

Similarly, the per-unit max power for each load port is given by

$$P_{\mathrm{MAB\_L\_max\_pu}} = \frac{2}{n}[m\psi(\phi) + r\psi(\beta)]. \quad (22)$$

The rated power of each port will result from the analysis of all the valid combinations of m, q, and r to find the worst case scenario. The approach developed herein will be illustrated through the analysis of the QAB converter in the next section.

III. QAB CONVERTER

Since the QAB converter has been selected for the implementation of the SST dc–dc stage, it will be analyzed herein following the approach developed for the MAB converter in the previous section. In [14], the authors briefly introduce the QAB converter; however, no experimental results have been provided to date. The switching model of the QAB converter is shown in Fig. 4 while its "Δ" equivalent ac circuit referred to port 1 is shown in Fig. 12, where the involved link inductances can be calculated with (6).

Based on Fig. 12, the idealized steady-state QAB waveforms for unity-dc-conversion ratios are illustrated in Fig. 13. The bottom two plots show the currents i_j at the dc side of the QAB ports, as defined in Fig. 5, along with their corresponding CCA values I_j. The gyrator-based average model for the QAB converter is presented in Fig. 14, where the involved gyration gains can be calculated by using (10).

When the max QAB link power has been reached between any two ports, the direction of the QAB power flow depends on the number of source, forwarding, and load ports. Fig. 15 illustrates the power flow for different operating scenarios. The required phase-shift angle α_{QAB} can be obtained from solving (23). It is important to note that ports not sinking or sourcing power will automatically operate as forwarding ports. The only
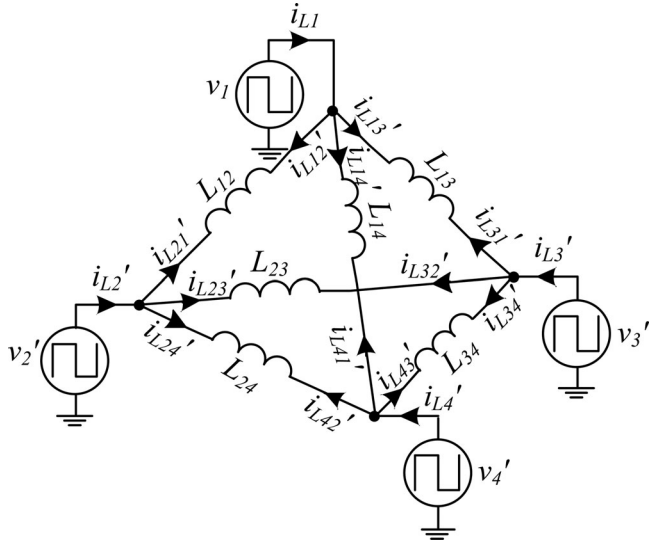
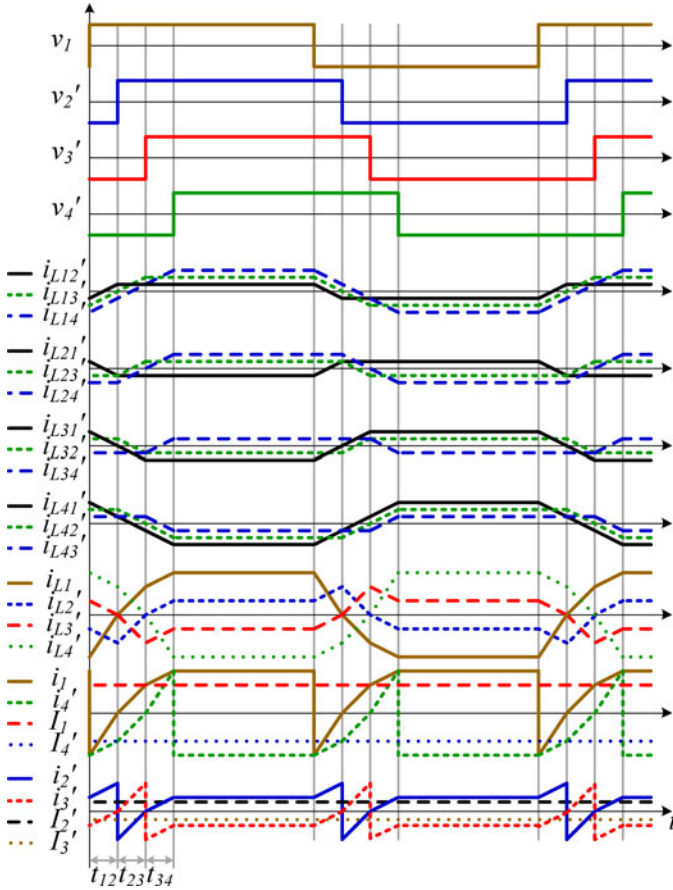Fig. 12. QAB "Δ" equivalent ac circuit referred to port 1.

Fig. 13. Idealized steady-state QAB switching waveforms for unity-dc-conversion ratios and equal link inductances.

way a QAB converter can have ports with no participation in the power flow is by turning it into a TAB or a DAB converter [14]

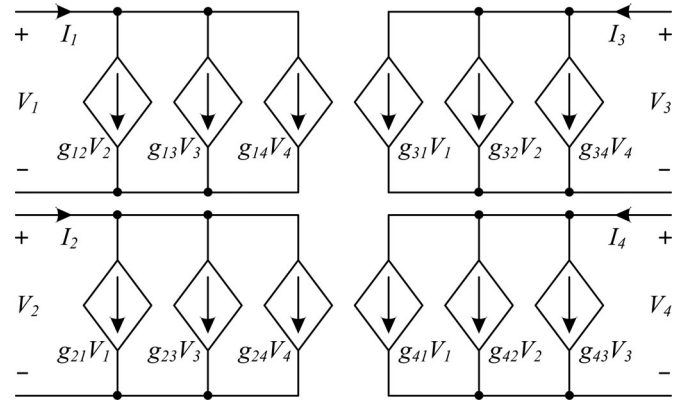$$\phi = \alpha_{\mathrm{QAB}} + \psi^{-1}\left(2\psi\left(\alpha_{\mathrm{QAB}}\right)\right). \tag{23}$$

Fig. 14. QAB gyrator-based average model.

$$-\psi(\phi)/2 \quad -\psi(\phi/2)/2 \quad \cdots \psi(\alpha_{QAB})/2$$
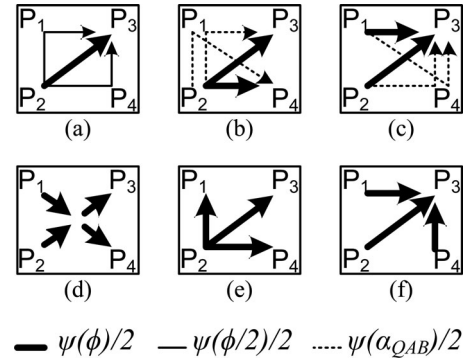
Fig. 15. QAB power-flow scenarios at max power levels: (a) one-source-one-load, (b) one-source-two-load, (c) two-source-one-load, (d) two-source-two-load, (e) one-source-three-load, and (f) three-source-one-load.

Depending on the particular application, some QAB ports might not be allowed to operate in all the scenarios depicted in Fig. 15, e.g., the PV port can only source power in steady state for the proposed SST topology; therefore, the ports associated with the grid and the battery cannot simultaneously source power under the scenario represented in Fig. 15(d), nor can either of them source power under the scenario represented in Fig. 15(e).

Based on (17), when $n = 4$, the max QAB link power in per unit is found to be

$$P_{\mathrm{QAB\_Link\_max\_pu}} = \frac{1}{2}\psi\left(\phi\right). \tag{24}$$

When operating in the one-source-one-load scenario, as in Fig. 15(a), the total max QAB power in per unit is

$$P_{\mathrm{QAB\_1S\_1L\_max\_pu}} = \frac{1}{2}\psi\left(\phi\right) + \psi\left(\frac{\phi}{2}\right). \tag{25}$$

For both scenarios operating with one forwarding port, that is, one-source-two-load and two-source-one-load, as in Fig. 15(b) and (c), respectively, the total max QAB power in per unit is

$$\begin{aligned} P_{\mathrm{QAB\_1S\_2L\_max\_pu}} &= P_{\mathrm{QAB\_2S\_1L\_max\_pu}} \\ &= \psi\left(\phi\right) + \psi\left(\alpha_{\mathrm{QAB}}\right). \end{aligned} \tag{26}$$

The total max QAB power in per unit when operating in the two-source-two-load scenario, as in Fig. 15(d), is found to be
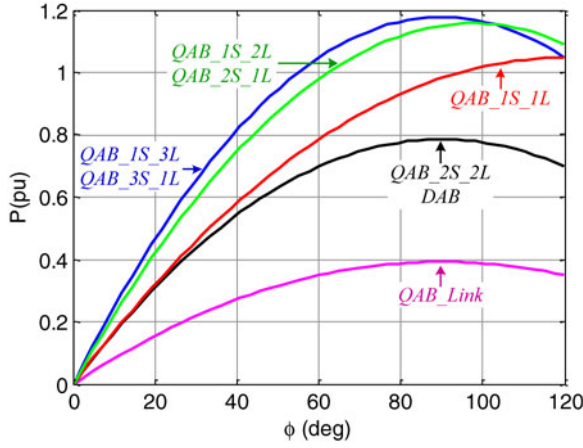
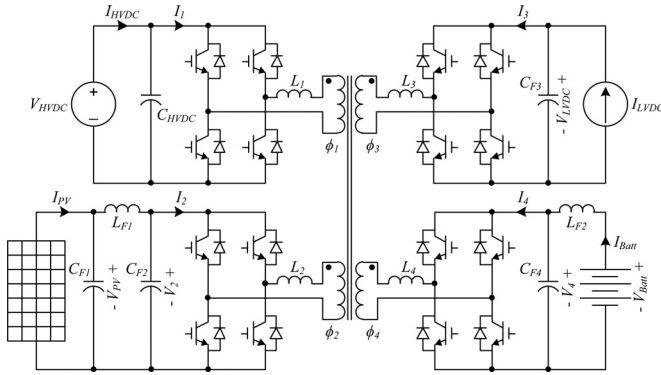Fig. 16.　QAB power curves to determine power rating of source and load ports.

Fig. 17.　SST dc–dc stage switching model.

the same as that of the DAB converter as follows:

$$P_{\text{QAB\_2S\_2L\_max\_pu}} = P_{\text{DAB\_max\_pu}} = \psi(\phi). \quad (27)$$

Finally, the total max QAB power in per unit for both the one-source-three-load and three-source-one-load scenarios, as in Fig. 15(e) and (f), respectively, is

$$P_{\text{QAB\_1S\_3L\_max\_pu}} = P_{\text{QAB\_3S\_1L\_max\_pu}} = \frac{3}{2}\psi(\phi). \quad (28)$$

The total max QAB power in per unit for each scenario has been plotted as a function of ϕ in Fig. 16. The rated power for each QAB port can be determined depending on the corresponding worst case scenario it may operate. Fig. 16 suggests that, when the QAB converter only operates in the one-source-one-load scenario, turning the QAB converter into a DAB converter in order to minimize losses may result in a reduced capacity, depending on the selected ϕ.

IV. SST DC–DC STAGE

The control design for the dc–dc stage of the proposed QAB-based SST topology is presented in this section. The switching model of the considered system is shown in Fig. 17. Since the current at the dc side of each port results from the rectification of its corresponding ac current, it has a ripple with twice the

switching frequency. In order to prevent the ripple currents from reaching the PV and the battery, *CLC* and *LC* filters are added to their corresponding ports.

The HVDC link, regulated by the rectifier stage, acts as a slack dc bus in order to balance the QAB power flow, including the losses. At the LVDC side, the inverter is modeled with an independent dc-current source that is negative when discharging the LVDC link capacitor. A more accurate model requires this current to change in order to keep the load power constant.

The PV voltage is to be regulated to a reference value provided by a maximum-power-point-tracking stage, the LVDC voltage is to be regulated to a fixed value, and the battery current is to be regulated to a reference value provided by a battery-management stage. The selected control variables for the above outputs are the phase-shift angles ϕ_2, ϕ_3, and ϕ_4, respectively, while ϕ_1 is fixed to zero. Since the HVDC voltage is regulated by the rectifier to a fixed value, and the PV and battery voltages are assumed to have variations of only $\pm 20\%$ of their rated value for this type of application [19]–[22], duty-ratio control will not be considered herein in order to ensure ZVS operation of the QAB converter at light loads [10].

A. Plant Modeling

The nominal plant is assumed to be lossless and only the predominant dynamics associated with the filters at the dc side of each port have been considered herein. The model of the QAB converter is represented by the nonlinearity Ψ defined as

$$I = \begin{bmatrix} I_2 & I_3 & I_4 \end{bmatrix}^T = \Psi(\Phi), \quad \Phi = \begin{bmatrix} \phi_2 & \phi_3 & \phi_4 \end{bmatrix}^T \quad (29)$$

where the vector I only includes the CCA currents that drive the corresponding plant outputs. G_Ψ is the transfer function matrix of the linearized model of the QAB converter around the operating point OP with its main diagonal and off-diagonal entries given by

$$G_{jj} = \left. \frac{\partial I_j}{\partial \phi_j} \right|_{\text{OP}} = \sum_{l \neq j}^4 \frac{N_1^2}{N_j N_l} \frac{V_l^{\text{OP}}}{2\pi f_s L_{jl}} \left[1 - \frac{2\left| \phi_j^{\text{OP}} - \phi_l^{\text{OP}} \right|}{\pi} \right] \quad (30)$$

and

$$G_{jk} = \left. \frac{\partial I_j}{\partial \phi_{k \neq j}} \right|_{\text{OP}} = -\frac{N_1^2}{N_j N_k} \frac{V_k^{\text{OP}}}{2\pi f_s L_{jk}} \left[1 - \frac{2\left| \phi_j^{\text{OP}} - \phi_k^{\text{OP}} \right|}{\pi} \right] \quad (31)$$

respectively, where j, $k \in \{2, 3, 4\}$, and $l \in \{1, 2, 3, 4\}$. Additionally, the transfer functions of the filters at the dc side of the QAB ports are defined as

$$G_{\text{PV}}(s) = \frac{V_{\text{PV}}(s)}{I_2(s)}, \quad G_{\text{LVDC}}(s) = \frac{V_{\text{LVDC}}(s)}{I_3(s)}$$

$$G_{\text{Batt}}(s) = \frac{I_{\text{Batt}}(s)}{I_4(s)}. \quad (32)$$

Due to the cross-coupling characteristics of the QAB converter, a decoupling stage can be implemented at the plant input through the inverse of G_Ψ [23]. This is depicted in Fig. 18(a), where $G_C = \text{diag}[G_{C2}, G_{C3}, G_{C4}]$ is the controller transfer function matrix; δE is the variation on the error vector; ΔI_{est} is
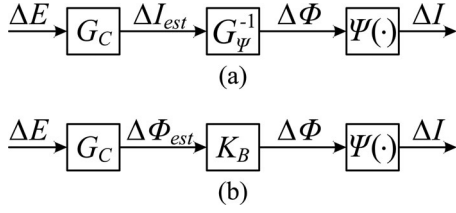
Fig. 18. QAB control strategies: (a) control-loop decoupling through the inverse of the plant-gain matrix and (b) manipulation of controls direction through the Bump-transferring matrix.

an estimate of ΔI, i.e., the variation on I, since G_Ψ comes from a linear approximation of the plant; and $\Delta\Phi$ is the variation on Φ. Furthermore, due to the nonlinear characteristics of the QAB converter, for an extended operating region, a gain-scheduling technique can be implemented to update the entries of G_Ψ [12].

An alternative approach to minimize the interaction between the control loops due to the cross-coupling characteristics of the QAB converter is selecting different bandwidths for the control loops [11]. As a result, the loop with the higher bandwidth will determine the direction of $\Delta\Phi$ during transients. Furthermore, a technique briefly introduced in [13] to manipulate the direction of $\Delta\Phi$ in order to improve the dynamic performance of a particular TAB port can be extended to the QAB converter. This is depicted in Fig. 18(b), where $\Delta\Phi_{\text{est}} = [\Delta\phi_{2\text{est}}, \Delta\phi_{3\text{est}}, \Delta\phi_{4\text{est}}]^T$ is an estimate of $\delta\Phi$ and K_B is defined herein as the Bump-transferring matrix.

B. Bump-Transferring Matrix

The selection of K_B consists in setting that direction the QAB power flow should follow when power in injected from any port. Considering that the power is drawn instead results in the same matrix. For this analysis, the possible power flow scenarios identified in Fig. 15 will be applied to the power variations. This technique enables a port to transfer the power variation (or power bump) onto the ports with lower bandwidth loops. The loop with the lowest bandwidth can only transfer the power variation to the slack port, which in this application is the HVDC port. This occurs because the proportions in which the power variation is divided among the QAB links, as indicated in Fig. 15, tends to be dynamically modified by the control loops working at different bandwidths.

When the direction of $\Delta\Phi_{\text{est}}$ is not altered, i.e., K_B equals the identity matrix, and power is injected at a high-bandwidth port, the power flow tends to follow the direction shown in Fig. 15(e) being divided among the other three ports. On the other hand, if the power is drawn, the direction is as shown in Fig. 15(f).

In order to redirect the power variation to a single port, as in figure Fig. 15(a), the K_B matrix is obtained in three steps. Given that ϕ_1 is fixed to zero, in order to transfer the power variation from the PV port onto the HVDC port, then

$$\Delta\Phi = \begin{bmatrix} \Delta\phi \\ \Delta\phi/2 \\ \Delta\phi/2 \end{bmatrix} = \begin{bmatrix} 1 & & \\ 0.5 & 1 & \\ 0.5 & & 1 \end{bmatrix} \begin{bmatrix} \Delta\phi \\ 0 \\ 0 \end{bmatrix}. \quad (33)$$

Similarly, in order to transfer the power variation from the LVDC port onto the HVDC port, then

$$\Delta\Phi = \begin{bmatrix} \Delta\phi/2 \\ \Delta\phi \\ \Delta\phi/2 \end{bmatrix} = \begin{bmatrix} 1 & 0.5 & \\ & 1 & \\ & 0.5 & 1 \end{bmatrix} \begin{bmatrix} 0 \\ \Delta\phi \\ 0 \end{bmatrix}. \quad (34)$$

In order to transfer the power variation from the battery port onto the HVDC port, then

$$\Delta\Phi = \begin{bmatrix} \Delta\phi/2 \\ \Delta\phi/2 \\ \Delta\phi \end{bmatrix} = \begin{bmatrix} 1 & & 0.5 \\ & 1 & 0.5 \\ & & 1 \end{bmatrix} \begin{bmatrix} 0 \\ 0 \\ \Delta\phi \end{bmatrix}. \quad (35)$$

Finally, after combining these three partial results, power variations will always get transferred to the HVDC port by using

$$K_B = \begin{bmatrix} k_{22} & k_{23} & k_{24} \\ k_{32} & k_{33} & k_{34} \\ k_{42} & k_{43} & k_{44} \end{bmatrix} = \begin{bmatrix} 1 & 0.5 & 0.5 \\ 0.5 & 1 & 0.5 \\ 0.5 & 0.5 & 1 \end{bmatrix}. \quad (36)$$

When the three SST stages are interconnected, the single-phase rectifier and the single-phase inverter inject 120-Hz-ripple currents into their corresponding dc links that are then propagated to the rest of the ports. A practical selection of K_B is to minimize the effect of these ripple currents on the HVDC, LVDC, and PV voltages; which may allow for a reduction on the size of the filters. This can be achieved by the transferring any power variation onto the battery port. In order to transfer the power variation from the PV port onto the battery port, then

$$\Delta\Phi = \begin{bmatrix} \Delta\phi \\ 0 \\ -\Delta\phi \end{bmatrix} = \begin{bmatrix} 1 & & \\ & 1 & \\ -1 & & 1 \end{bmatrix} \begin{bmatrix} \Delta\phi \\ 0 \\ 0 \end{bmatrix}. \quad (37)$$

In order to transfer the power variation from the LVDC port onto the battery port, then

$$\Delta\Phi = \begin{bmatrix} 0 \\ \Delta\phi \\ -\Delta\phi \end{bmatrix} = \begin{bmatrix} 1 & & \\ & 1 & \\ & -1 & 1 \end{bmatrix} \begin{bmatrix} 0 \\ \Delta\phi \\ 0 \end{bmatrix}. \quad (38)$$

In order to transfer the power variation from the HVDC port onto the battery port, (35) can be used. After combining these partial results, the required K_B is given by

$$K_B = \begin{bmatrix} 1 & & 0.5 \\ & 1 & 0.5 \\ -1 & -1 & 1 \end{bmatrix}. \quad (39)$$

In summary, the approach presented herein takes into account the cross-coupling characteristics of the QAB converter to improve the dynamical performance of a selected port.

C. Control Loops

The block diagram in Fig. 19 shows the single-input-single-output type of control loop for the PV voltage implemented
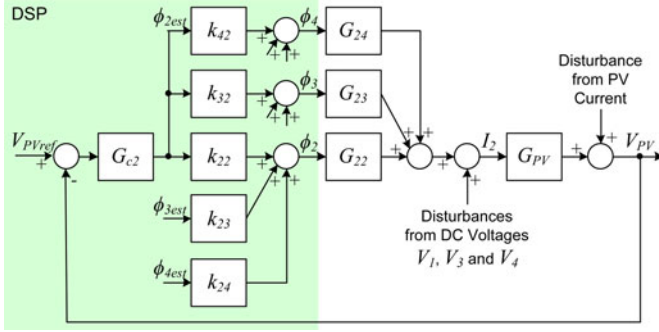
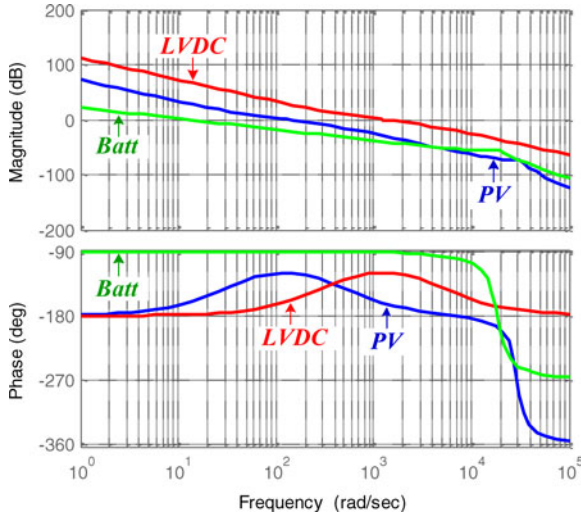Fig. 19.   Simplified PV voltage control loop.

Fig. 20.   Bode plot of SST dc–dc stage open-loop gains.

TABLE I
SYSTEM ELECTRICAL PARAMETERS

| Description	Symbol	Value
High-voltage-DC link voltage	V_{HVDC}	48 V
Low-voltage-DC link voltage	V_{LVDC}	48 V
PV voltage	V_{PV}	48 V
Battery voltage	V_{Batt}	48 V
Ports Current Rating	I_{Rating}	5 A
Port 1 leakage inductance	L_1	0.851 pu
Port 2 leakage inductance	L_2	0.851 pu
Port 3 leakage inductance	L_3	0.851 pu
Port 4 leakage inductance	L_4	0.851 pu
CLC filter inductance	L_{F1}	0.151 pu
LC filter inductance	L_{F2}	0.191 pu
High-voltage-DC link capacitance	C_{HVDC}	200 µF
CLC filter capacitance 1	C_{F1}	200 µF
CLC filter capacitance 2	C_{F2}	200 µF
Low-voltage-DC link capacitance	C_{F3}	200 µF
LC filter capacitance	C_{F4}	200 µF
Maximum phase-shift angle	ϕ	90°
Switching frequency	f_s	20 kHz
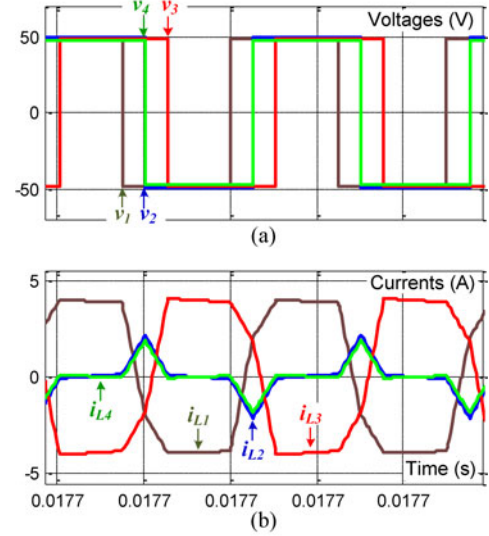
Fig. 21.   Simulation results: QAB steady-state switching waveforms for $\phi_2 = -38°$, $\phi_3 = -76°$, and $\phi_4 = -38°$.

herein. The gains associated with the feedback-signal conditioning, as well as the DSP digital-to-analog conversion and pulsewidth modulation (PWM) modules have been intentionally omitted for simplicity. The control loops for the LVDC voltage and the battery current share the same structure. In the event that its saturation limits implemented on the DSP are reached, a controller may try to drive the phase-shift angles of the slower loops through the entries of the K_B matrix. In order to avoid this, it may require forcing K_B to be the identity matrix.

As seen in the Bode plot in Fig. 20, the LVDC loop is selected to be the fastest and the battery loop to be the slowest of the SST dc–dc stage in Fig. 17. The entries of G_C have been designed with the k-factor technique [24] with bandwidths of 200, 20, and 2 Hz for Gc3, Gc2, and Gc4, respectively, and phase margin of 60° for all of them. Alternatively, a multiple-input-multiple-output type of control loop can be considered in order to incorporate the dc voltages as plant state variables [25], [26].

V. SIMULATION RESULTS

The selected simulation package is MATLAB/Simulink complemented with PLECS® blockset. Based on Fig. 17, the system electrical parameters are listed in Table I. The base inductance, obtained from the switching frequency, voltage, and current rating, is 76.4 µH. The QAB switching waveforms for $\phi_2 = -38°$,

$\phi_3 = -76°$, and $\phi_4 = -38°$ are shown in Fig. 21. For the simulation of the close-loop operation, a step load at the LVDC link is applied to the system. The transient response when K_B equals the identity matrix is seen in Fig. 22. It can be observed that, following the disturbance, the power variation is distributed among the remaining ports. This causes the PV voltage to dip. In steady state, the power is balanced by the HVDC link.

When K_B is selected to transfer the power variation onto the HVDC port, the transient response is seen in Fig. 23. It can be observed that the current from the HVDC link is forced to increase to meet the current demanded by the load with minimal undershoot on the PV and battery currents. Fig. 24 shows the transient response when K_B is selected to transfer the power
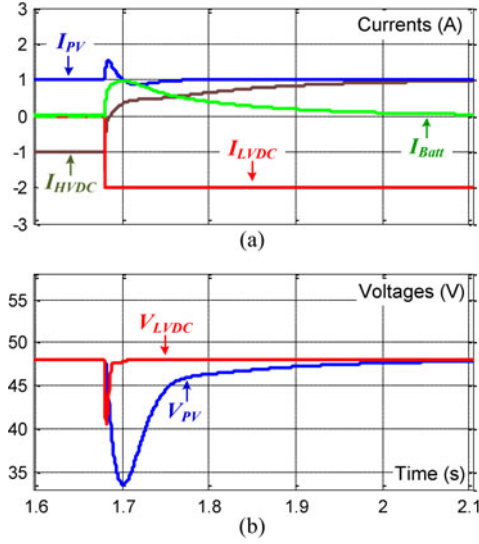
Fig. 22. Simulation results: SST dc–dc stage transient response to a step load when K_B equals the identity matrix.
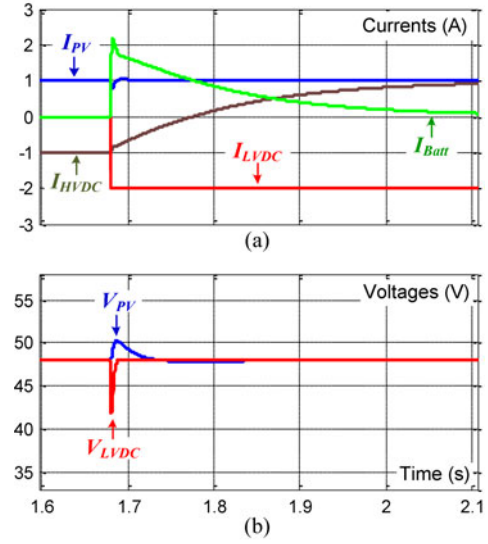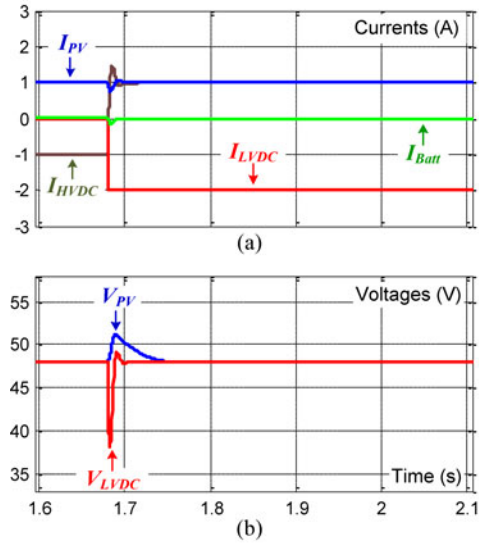

Fig. 23. Simulation results: SST dc–dc stage transient response to a step load when the power variation is transferred onto the HVDC link.

Fig. 24. Simulation results: SST dc–dc stage transient response to a step load when the power variation is transferred onto the storage.

Fig. 25. Experimental results: QAB steady-state switching waveforms for $\phi_2 = -38°$, $\phi_3 = -76°$, and $\phi_4 = -38°$.

variation onto the battery port. As a result, following the disturbance, the battery is forced to supply the current demanded by the load before slowly returning to its initial steady state.

As seen from the simulation results, The QAB dc-side currents are directly controlled through the phase-shift angles both during transients as well as during steady state, thus ensuring the transformer amp-turn balancing at the QAB ac side. During transients, the QAB currents are shared depending on the selection of K_B, as seen in Fig. 22 through Fig. 24. During steady state, the QAB currents are shared depending on the controls set point.
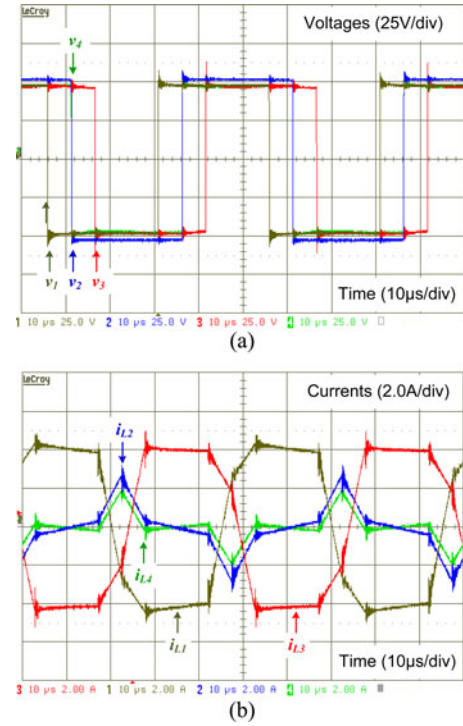
VI. EXPERIMENTAL RESULTS

A prototype with the electrical parameters listed in Table I has been developed for validation purposes. The voltage rating is set to 48 V for all dc ports herein; however, the HF-transformer turns ratio can be modified for different voltage ratings. The controller is implemented on a Texas InstrumentsTMS320F28335 DSP.

The measured QAB switching waveforms for $\phi_2 = -38°$, $\phi_3 = -76°$, and $\phi_4 = -38°$ are shown in Fig. 25. They closely
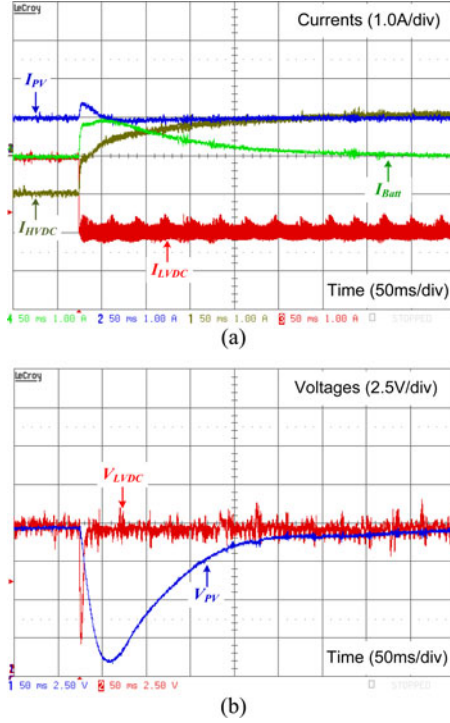
Fig. 26.   Experimental results: SST DC-DC stage transient response to a step load when K_B equals the identity matrix.
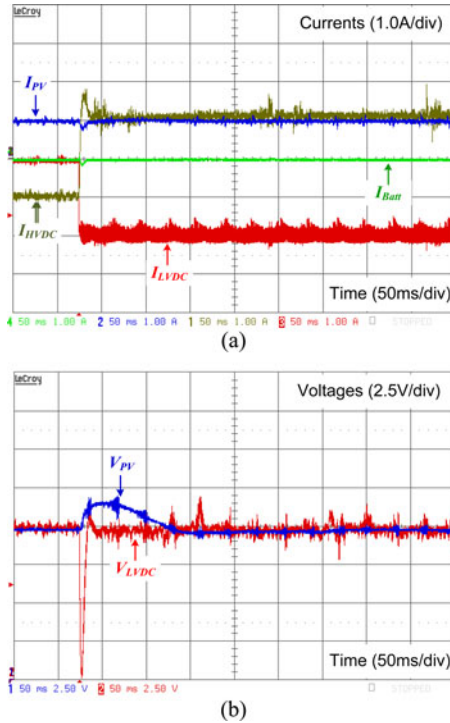

Fig. 27.   Experimental results: SST dc–dc stage transient response to a step load when the power variation is transferred onto the HVDC link.

Fig. 28.   Experimental results: SST dc–dc stage transient response to a step load when the power variation is transferred onto the storage.

match those from the simulation results in Fig. 21. For the verification of the closed-loop operation, a step load at the LVDC link is applied. The transient response when K_B equals the identity matrix is seen in Fig. 26, whereas the transient responses when K_B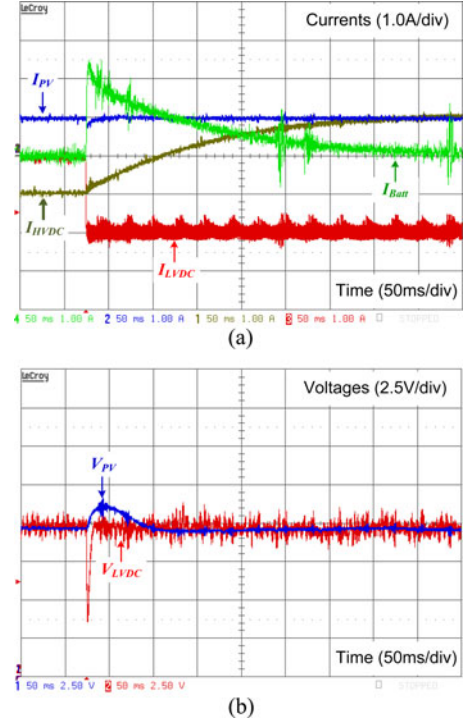 is selected to transfer the power variation onto the HVDC port and to the battery port are seen in Figs. 27 and 28, respectively. These experimental results verify those from the simulation shown in Fig. 22 through Fig. 24 for each K_B value, respectively.

VII.   CONCLUSION

A SST topology based on a QAB converter that provides isolation for the load, as well as DG and storage has been proposed herein. A gyrator-type large-signal average model has been developed for a general MAB converter and used to speed up the simulation of the dc–dc stage of the QAB-based SST. The expressions to determine the power rating of an MAB port have been derived and used to determine the power rating of the QAB ports considering the operating characteristics of the SST application. A control technique that takes into account the cross-coupling characteristics of the QAB converter has been introduced herein. This technique allows improving the dynamic performance of the HVDC voltage regulation of the SST. The dynamic performance of the control strategy has been verified through extensive simulation of both switching and average models. Experimental results have been provided for validation purposes.

REFERENCES

[1] R. Hassan and G. Radman, "Survey on smart grid," in *Proc. IEEE Southeast Con*, Mar. 18–21, 2010, pp. 210–213.
[2] A. Q. Huang and J. Baliga, "FREEDM system: Role of power electronics and power semiconductors in developing an energy internet," in *Proc. 21st Int. Symp. Power Semicond. Devices ICs*, Jun. 14–18, 2009, pp. 9–12.

[3] G. T. Heydt, "Future renewable electrical energy delivery and management systems: Energy reliability assessment of FREEDM systems," in *Proc. IEEE Power Energy Soc. Gen. Meet.*, Jul. 25–29, 2010, pp. 1–4.

[4] G. G. Karady and X. Liu, "Fault management and protection of FREEDM systems," in *Proc. IEEE Power Energy Soc. Gen. Meet.*, Jul. 25–29, 2010, pp. 1–4.

[5] T. Zhao, L. Yang, J. Wang, and A. Q. Huang, "270 kVA solid state transformer based on 10 kV SiC power devices," in *Proc. IEEE Electric Ship Technol. Symp.*, May 21–23, 2007, pp. 145–149.

[6] S. Falcones, X. Mao, and R. Ayyanar, "Topology comparison for solid state transformer implementation," in *Proc. IEEE Power Energy Soc. Gen. Meet.*, Jul. 25–29, 2010, pp. 1–8.

[7] S. Falcones, X. Mao, and R. Ayyanar, "Simulink block-set for modeling distribution systems with solid state transformer," in *Proc. Future Renewable Elect. Energy Distrib. Manage. Annu. Conf.*, Raleigh, NC, May 18–19, 2009, pp. 181–184.

[8] G. Wang, S. Baek, J. Elliott, A. Kadavelugu, F. Wang, X. She, S. Dutta, Y. Liu, T. Zhao, W. Yao, R. Gould, S. Bhattacharya, and A. Q. Huang, "Design and hardware implementation of Gen-1 silicon based solid state transformer," in *Proc. 26th Annu. IEEE Appl. Power Electron. Conf. Expo.*, Mar. 6–11, 2011, pp. 1344–1349.

[9] H. Tao, A. Kotsopoulos, J. L. Duarte, and M. A. M. Hendrix, "Family of multiport bidirectional DC–DC converters," *IEE Proc.—Electric Power Appl.*, vol. 153, no. 3, pp. 451–458, May 2006.

[10] R. W. A. A. De Doncker, D. M. Divan, and M. H. Kheraluwala, "A three-phase soft-switched high-power-density DC/DC converter for high-power applications," *IEEE Trans. Ind. Appl.*, vol. 27, no. 1, pp. 63–73, Jan./Feb. 1991.

[11] H. Tao, A. Kotsopoulos, J. L. Duarte, and M. A. M. Hendrix, "A soft-switched three-port bidirectional converter for fuel cell and supercapacitor applications," in *Proc. IEEE 36th Power Electron. Spec. Conf.*, Jun. 2005, pp. 2487–2493.

[12] C. Zhao and J. Kolar, "A novel three-phase three-port UPS employing a single high-frequency isolation transformer," in *Proc. Power Electron. Specialists Conf.*, vol. 6, Jun. 2004, pp. 4135–4141.

[13] S. Falcones and R. Ayyanar, "Simple control design for a three-port DC-DC converter based PV system with energy storage," in *Proc. 25th Annu. IEEE Appl. Power Electron. Conf. Expo.*, Feb. 21–25, 2010, pp. 2149–2153.

[14] M. Qiang, W. Wei-yang, and X. Zhen-lin, "A multi-directional power converter for a hybrid renewable energy distributed generation system with battery storage," in *Proc. CES/IEEE 5th Int. Power Electron. Motion Control Conf.*, Aug. 14–16, 2006, vol. 3, pp. 1–5.

[15] Q. Chen, F. C. Lee, J. Z. Jiang, and M. M. Jovanovic, "A new model for multiple-winding transformer," in *Proc. 25th Annu. IEEE Power Electron. Spec. Conf. Rec.*, Jun. 20–25, 1994, vol. 2, pp. 864–871.

[16] M. Ehsani, I. Husain, and M. O. Bilgic, "Power converters as natural gyrators," *IEEE Trans. Circuits Syst. I: Fundam. Theory Appl.*, vol. 40, no. 12, pp. 946–949, Dec. 1993.

[17] H. Tao, J. L. Duarte, and M. A. M. Hendrix, "Three-port triple-half-bridge bidirectional converter with zero-voltage switching," *IEEE Trans. Power Electron.*, vol. 23, no. 2, pp. 782–792, Mar. 2008.

[18] D. Liu, H. Li, and L. D. Marlino, "Design of a 6 kW multiple-input bi-directional DC-DC converter with decoupled current sharing control for hybrid energy storage elements," in *Proc. IEEE 22nd Annu. Appl. Power Electron. Conf.*, Feb. 25/Mar. 1, 2007, pp. 509–513.

[19] H. Haeberlin, "Optimum DC operating voltage for grid-connected PV plants," in *Proc. 20th Eur. Photovoltaic Conf.*, Barcelona, Spain, 2005, pp. 2253–2256.

[20] U. Boke, "A simple model of photovoltaic module electric characteristics," in *Proc. Eur. Conf. Power Electron. Appl.*, Sep. 2007, pp. 1–8.

[21] M. Coleman, C. K. Lee, C. Zhu, and W. G. Hurley, "State-of-charge determination from EMF voltage estimation: Using impedance, terminal voltage, and current for lead-acid and lithium-ion batteries," *IEEE Trans. Ind. Electron.*, vol. 54, no. 5, pp. 2550–2557, Oct. 2007.

[22] D. Guasch and S. Silvestre, "Dynamic battery model for photovoltaic applications," *Progress Photovoltaics: Res. Appl.*, vol. 11, no. 3, pp. 193–206, Jan. 2003.

[23] W. L. Luyben, "Distillation decoupling," *Am. Inst. Chemical Eng.*, vol. 16, no. 2, pp. 198–203, Mar. 1970.

[24] N. Mohan, T. M. Undeland, and W. P. Robbins, *Power Electronics: Converters, Applications, and Design*, 2nd ed. New York: Wiley, 1995.

[25] A. A. Rodriguez, *Analysis and Design of Multivariable Feedback Control Systems*. Tempe, AZ: Control3D, LLC, 2003.

[26] D. S. Naidu, *Optimal Control Systems*. Boca Raton, FL: CRC Press, 2003.

Sixifo Falcones (S'09–M'12) received the B.S. degree, in 1999, in electrical engineering from Escuela Superior Politecnica del Litoral, Guayaquil, Ecuador, and the M.S. and Ph.D. degrees from Arizona State University, Tempe, in 2005 and 2011, respectively.

He is currently an Associate Professor at the Escuela Superior Politecnica del Litoral. His research interests include multiport converters for integration of distributed renewable energy resources, modular power converters, solid-state transformers, and microgrids.

Rajapandian Ayyanar (M'00–SM'06) received the M.S. degree from the Indian Institute of Science, Bangalore, India, and the Ph.D. degree from the University of Minnesota, Minneapolis.

He is currently an Associate Professor at the Arizona State University, Tempe, AZ. He has many years of industrial experience designing switch mode power supplies. His current research interests include topologies and control methods for switch mode power converters, fully modular power system architecture, new pulsewidth modulation techniques, design of power conversion systems and distribution systems for large scale, distributed integration renewable energy resources—mainly solar PV and wind, and power electronics applications in enabling "smart grid."

Dr. Ayyanar received the ONR Young Investigator Award in 2005. He serves as an Associate Editor for the IEEE TRANSACTIONS ON POWER ELECTRONICS.

Xiaolin Mao (S'04–M'06) received the B.S. and M.S. degrees from Tsinghua University, Beijing, China in 1997 and 2000, respectively, and the Ph.D. degree from Arizona State University, Tempe, in 2005, all in electrical engineering.

From 2006 to 2011, he was a Postdoctoral Researcher and Assistant Research Scientist at Arizona State University. He is currently a Power Electronics Engineer at Power-One, Renewable Energy Solutions, LLC, Camarillo, CA. His research interests include high-power ac–dc converters, design and modeling of power conversion systems in applications for distributed renewable energy resources, modular power converters, and new pulsewidth modulation techniques.